



Delayed detached eddy simulation method for breaking bow waves of a surface combatant model with different trim angle

Dingkun Wu, Jianhua Wang, Decheng Wan^{*}

Computational Marine Hydrodynamics Lab (CMHL), School of Naval Architecture, Ocean and Civil Engineering, Shanghai Jiao Tong University, Shanghai, 200240, China

ARTICLE INFO

Keywords:

Breaking bow wave
Interface-compression algebraic VOF
DDES method
DTMB 5415 ship model
Trim angle

ABSTRACT

Sailing attitudes vary with different loading conditions for ships sailing in open sea, and the trim angle, either by bow or by stern, exerts considerable impact on the flow field around the ship. Currently, attention has primarily been focused on hull resistance and wave patterns while few studies have touched upon breaking bow wave under different trim conditions. This study aims to analyze the breaking bow wave of a surface combatant model with a length of 5.72 m DTMB (name of a surface combatant model) under different sailing attitudes at $Fr = 0.35$. The Delayed Detached Eddy Simulation (DDES) approach was adopted to study the breaking bow wave features such as plunging jet and air entrainment. The interface-compression algebraic Volume Of Fluid (VOF) method in OpenFOAM was used to capture the free surface. The Computational Fluid Dynamics (CFD) approach was firstly validated by comparing hull resistance and wave contour with the available experimental data. The study then delves into the influence of trim angles on breaking bow waves through simulations of the different conditions, i. e., 1 deg trim by bow, test condition and 1 deg trim by stern. The wave contour, breaking wave profile, vorticity field and the wake field at several transverse sections are then compared in three trim conditions, followed by an analysis of the initial evolution of bow wave breaking based on the turbulent kinetic energy and the vorticity field at four cross sections. The results suggest that trim by bow makes free surface sharper and wave amplitude larger in the breaking bow wave region. The reason is that trim by bow enlarges the attack angle of the bow, thus energizing the bow wave and generating a more violent free surface of bow wave breaking.

1. Introduction

Formed in the high-pressure area at the bow of ship at high speed, the violent breaking bow wave, including spray, foam and bubbles, has impact on hull resistance and remains one of the most complex problems in ship hydrodynamics. In previous studies, the features of breaking bow waves are observed via experiment method. Dong et al. (1997) measured the breaking bow wave structure of DTMB 5512 ship model via PIV method and compared the vortex field and the velocity field at different speeds. The results indicated that the convective vortex appears under the free surface at $Fr = 0.28$ or on the surface of the ship at $Fr = 0.45$. Although the convective vortex was observed via experiment method, the causes and the details of vortex formation during breaking bow wave were not analyzed. Olivieri et al. (2003) examined the phenomenon of bow wave breaking of the INSEAN 2340 model at high Fr number, and measured the root mean square value of wave height and the velocity field at sections $X/L_{pp} = 0.15$ and 0.2 by using a probe to

enrich the data of breaking bow wave of benchmark model. Liu et al. (2020) designed a new type of bow appendage to restrain the peak of bow wave. The ship model experiments were conducted to verify the effects of the bow appendage on reducing the resistance of ship model. Experimental results show that this bow appendage is able to restrain bow wave of the ship model and reduce the total resistance by more than 8% to the maximum extent. In despite of a growing body of experiments on breaking bow wave, details of fine flow field features such as free surface evolution and air entrainment were not measured accurately. It is very hard to capture the details of viscous flow fields during breaking bow wave via experiment method.

In recent years, Computational Fluid Dynamics (CFD) approach is widely used in flow field simulation. Numerical methods such as Reynolds-Averaged Navier-Stokes (RANS), Large Eddy Simulation (LES) and Direct Numerical Simulation (DNS) are used to solve breaking wave phenomenon. Deike et al. (2015) used DNS approach to simulate capillary effects on wave breaking, and proposed the use of Bond Number and wave steepness to determine the processes of wave

^{*} Corresponding author.

E-mail address: dcwan@sjtu.edu.cn (D. Wan).

Nomenclature part containing definitions for typical symbols

DDES	Delayed Detached Eddy Simulation
VOF	Volume Of Fluid
CFD	Computational Fluid Dynamics
EFD	Experimental Fluid Dynamics
RANS	Reynolds-Averaged Navier-Stokes
LES	Large Eddy Simulation
DNS	Direct Numerical Simulation
URANS	Unsteady Reynolds-Averaged Navier-Stokes
IDDES	Improved Delayed Detached Eddy Simulation
l_{pp}	Length between the perpendiculars
Fr	Froude number
C_p	Pressure resistance coefficient
C_v	Viscous resistance coefficient
C_{tm}	Total resistance coefficient
Q	Vortex identification criterion

breaking. The wave breaking initiation time as a function of these two parameters was determined and a phase diagram in terms of the Bond number is presented to distinguish gravity waves, spilling waves and plunging waves. Despite the fact that the DNS method can accurately simulate the complex flow field, its enormous computational effort makes it unsuitable for engineering calculations. Olivieri et al. (2007) predicted breaking bow wave phenomenon of ship model DTMB5415 by using RANS approach. The topologies of bow wave and shoulder wave were analyzed. Scars and velocity fields were compared well with experimental data. The results showed that the bow wave breaking included large free surface RMS, vortex and scars. Ren (Ren et al., 2018) simulated the breaking bow wave of KCS model under $Fr = 0.26$, $Fr = 0.3$ and $Fr = 0.35$ by using naoe-FOAM-SJTU solver. For the $Fr = 0.26$ case, the predicted resistance and wave patterns are in good agreement with the available experimental data. For the $Fr = 0.35$ case, the results show that violent wave overturning can be observed. Despite that the features such as plunging jet and scars were observed in this study, the air entrainment was invisible and the causes of vortex generation were ignored. Wang (Wang and Wan, 2017) performed numerical simulations of DTMB5415 model, solved the Navier-Stokes (N-S) equation based on the unsteady Reynolds-Averaged Navier-Stokes (URANS) method, and obtained cross-sectional vorticity field, velocity field, and more flow details. The simulation used 18M grids to predict breaking bow wave at $Fr = 0.35$. The results show that the CFD solution of ship resistance shows a good agreement with the experiment. The comparisons of velocity components at cross planes show that the present VOF based RANS method can accurately predict the wake region associated with breaking wave. Wilson and Stern (Wilson et al., 2007) used an unsteady single-phase level set RANS method to investigate breaking bow wave of DTMB5415 in calm water. Local overset grid was used to resolve the complex interfacial topologies, and a level set approach was extended to capture free surface during breaking wave. The paper provided the entire evolution of breaking bow wave and filled in gaps in previous experimental data (Olivieri et al., 2007). Apparently, RANS method has a considerable advantage in resistance calculation and computational efficiency, but it averages the N-S equation by time and smooths out the turbulent pulsations in the flow field, making the free surface solved by the RANS method rather smooth and a significant part of breaking bow waves largely unobservable.

By contrast, since the Detached Eddy Simulation (DES) method can effectively obtain the complex turbulent pulsations while saving the mesh in boundary layer, more and more researchers are trying to use DES methods to solve complex flow field problems in hydrodynamics. Li et al. (2020) carried out the simulation of ship flow field via the hybrid RANS/LES method and introduced an improved model for the complex

flow features such as overturning and breaking in the ship wake. It was concluded that this model could make the turbulent kinetic energy more fidelity in the transition from RANS to LES region and effectively improved the application of the DES method in such complex problems. Bhushan (Bhushan et al., 2013) simulated a single-phase flow over a surface combatant via four turbulence models. The results showed that DES method got more details than RANS method and both Spalart Allmaras based detached eddy simulation and $k-\omega$ based improved delayed detached eddy simulation predicted $<1\%$ resolved turbulence. Apart from that, DES method is also used in simulating breaking bow wave phenomenon. Wang and Wan (2019) used DES method with algebraic VOF model to simulate the two-phase flow field around JBC ship and compared the viscous flow field results predicted by DDES and improved delayed detached eddy simulation (IDDES) methods respectively. It can be observed that IDDES method can better predict the flow field of the whole ship, but there is unstable solution of turbulent kinetic energy equation near the free surface in DES result compared to that in RANS result. Kornev et al. (2019) developed a new hybrid URANS-LES method to study the two-phase flow field of a ship. Predicted results show that the transient velocity of the two-phase flow field around the ship varies significantly, and the effect of non-constant two-phase flow must be considered in the hydrodynamic analysis of the ship. Carrica (Carrica et al., 2010) used large-scale DES computations to simulate the DTMB5512 surface combatant under three speeds. The results show considerable improvement in the flow field during breaking bow wave, but values of forces and moments are smaller than those predicted via URANS model. Wang (Wang et al., 2020) predicted breaking bow wave phenomenon of KCS ship model by using URANS method and DDES method in OpenFOAM. The effects of ship speed were analyzed under $Fr = 0.28-0.41$. The results show that some small-scale free surface features can be captured via DDES method while the free surface vorticity dissipates quickly in the URANS simulation.

Breaking bow wave phenomenon of surface ships with high Froude numbers has been studied extensively worldwide. Most of the studies focus on the breaking bow wave in the positive floating condition. However, when a ship is sailing in the open sea, different loading conditions will cause different sailing attitudes. Trim by bow will make heading less stable and reduce the ship speed, while trim by stern can improve the rudder efficiency and propulsion efficiency. Both sailing attitudes will greatly change the flow field around ship especially in bow region. Le et al. (2021) studied the effect of trim on resistance of DTMB5415 model at three different drafts and two Fr numbers. The results showed that the variation of pressure resistance component was considerably larger than frictional resistance component under different trim conditions. Salma (Sherbaz and Duan, 2014) analyzed the tendency of each resistance component during the trim angle adjustment of container ship by numerical simulation. KCS hull total resistances and trim and sinkage computed values, in even keel condition, are compared with experimental data and results in reasonably good agreement. Both of the above two studies only focused on the effect of trim on resistance without considering that on breaking bow wave phenomenon. Oliver (Olivieri et al., 2007) predicted breaking bow wave of fixed model DTMB5415 under 0.0032 deg trim by bow condition, but the trim angle is too small to affect the evolution of free surface during breaking bow wave. The main purpose of that paper is to investigate the scars and vortex at $Fr = 0.35$. Nowadays, most studies have only investigated resistance variations and flow fields around ship and few studies investigate the breaking bow wave phenomenon of ship under large trim angle conditions. Admittedly, sailing attitudes can affect the free surface evolution in breaking bow wave region, and the breaking bow wave is closely related to ship resistance. Therefore, it is necessary to investigate the effect of different trim angle on bow wave breaking.

In this paper, accurate CFD method is used to investigate the breaking bow wave phenomenon under different trim conditions. The predicted resistance and wave contour in test condition are compared with the experimental data to verify the accuracy and reliability of the

CFD method. The wave contour, free surface outline, vorticity field and velocity field at several transverse cross sections are compared and analyzed under trim by bow and trim by stern conditions. The effect of trim on the vortex field and the turbulent kinetic energy in the bow region is analyzed to further analyze the flow mechanism.

2. Numerical method

The numerical simulation of breaking bow wave is performed based on CFD method by using in-house solver naoe-FOAM-SJTU (Zhao et al., 2020; Wang and Wan, 2018; Wang et al., 2019). In our previous study, Wang (Wang et al., 2020) has predicted breaking bow wave phenomenon of KCS ship model by using URANS method and DDES method. The results show that some small-scale free surface features such as scars and the second plunging jet can be captured via DDES method while the flow field region solved by URANS method is smooth and the features of breaking bow wave cannot be observed obviously. Therefore, in this study, DDES method is used to solve the N-S equation. Predicted hull resistance and wave elevation at $Fr = 0.35$ by DDES method are validated with the test data. In order to obtain the details of flow field during breaking wave, this paper uses the interface-compression algebraic VOF method with artificial compression term to capture free surface.

The governing equations used in this study are solved by DDES method in naoe-FOAM-SJTU and the equations are given as:

$$\nabla \cdot \mathbf{U} = 0 \quad (1)$$

$$\frac{\partial \rho \mathbf{U}}{\partial t} + \nabla \cdot (\rho(\mathbf{U} - \mathbf{U}_g)\mathbf{U}) = -\nabla p_d - \mathbf{g} \cdot \mathbf{x} \nabla \rho + \nabla \cdot (\mu_{eff} \nabla \mathbf{U}) + (\nabla \mathbf{U}) \cdot \nabla \mu_{eff} + f_\sigma \quad (2)$$

where \mathbf{U} is the velocity field and \mathbf{U}_g is the moving velocity of the grid. $p_d = p - \rho g x$ is dynamic pressure, which is the difference between the total pressure and the hydrostatic pressure. ρ is the flow density, \mathbf{g} the acceleration due to gravity, $\mu_{eff} = \rho(\nu + \nu_t)$ the effective dynamic viscosity coefficient, and ν and ν_t are the kinematic viscosity and turbulent eddy viscosity, respectively. f_σ is the surface tension term.

The principle of DES method is to use RANS method for the boundary layer near the wall and LES method for the separation flow region away from the wall. In this paper, we use SST $k - \omega$ two-equation model (Menter et al., 2003) to achieve the closure of the RANS equation. Where k is the turbulent kinetic energy of a fluid particle and ω is the characteristic dissipation rate of the fluid.

$$\frac{\partial k}{\partial t} + \nabla \cdot (Uk) = \tilde{G} - \beta^* k \omega + \nabla \cdot [(\nu + \sigma_k \nu_t) \nabla k] \quad (3)$$

$$\frac{\partial \omega}{\partial t} + \nabla \cdot (U\omega) = \gamma S^2 - \beta \omega^2 + \nabla \cdot [(\nu + \delta_\omega \nu_t) \nabla \omega] + (1 - F_1) CD_{k\omega} \quad (4)$$

In Eqn. (3), \tilde{G} is defined as:

$$\tilde{G} = \min(G, c_1 \beta^* k \omega), G = \nu_t S^2 \quad (5)$$

$$S = \sqrt{2S_{ij}S_{ij}} \quad (6)$$

$$S_{ij} = \frac{1}{2} [\nabla u + (\nabla u)^T] \quad (7)$$

where S is invariant measure of the strain rate and S_{ij} is strain rate tensor. F_1 is the blending function, which is used to blend $k - \epsilon$ model and $k - \omega$ model.

Since RANS/LES hybrid property of DES depends on the similarity of the turbulent dissipative terms of RANS and LES, RANS and LES regions can transit smoothly. However, in this region, turbulence viscosity may be incorrectly calculated because of switches of RANS and LES. To address such concerns, the DDES method is adopted to modify the tur-

bulent feature length by introducing a delay function.

$$f_d = 1 - \tanh((8r_d)^3) \quad (8)$$

where r_d is the delay factor, and the expression is given as:

$$r_d = \frac{\nu + \nu_t}{\sqrt{0.5(S^2 + \Omega^2)} \kappa d^2} \quad (9)$$

where $\kappa = 0.41$ is von Karman constant and d is the distance from wall.

$$L_{DDES} = L_{RANS} - f_d \max(0, L_{RANS} - L_{LES}) \quad (10)$$

According to above equations, f_d is equal to 0 in the boundary layer of the wall. The equations can ensure that DDES uses the RANS model to solve the flow field near the wall, which will prevent RANS model from being switched to LES model in a premature manner and makes Grid-Induced Separation solved. More details of the SST-DDES method in the naoe-FOAM-SJTU solver can be found in Zhao et al. (Zhao and Wan, 2016).

In this article, an interface-compression algebraic VOF method with artificial compression term is used to capture free surface of breaking bow wave. This method introduces a convection term, which provides a sharper interface. Firstly, the volume fraction transport equations for air and water are solved respectively.

$$\frac{\partial \alpha}{\partial t} + \nabla \cdot (U\alpha) = 0 \quad (11)$$

$$\frac{\partial (1 - \alpha)}{\partial t} + \nabla \cdot [U_g(1 - \alpha)] = 0 \quad (12)$$

where l and g denote water and air, respectively. Assuming that the effect of the velocities of water and air on evolution of free surface is positively related to their volume fraction. The effective velocity field in the whole flow field can be characterized as follow:

$$\mathbf{U} = \alpha \mathbf{U}_l + (1 - \alpha) \mathbf{U}_g \quad (13)$$

$$\frac{\partial \alpha}{\partial t} + \nabla \cdot (U\alpha) + \nabla \cdot [U_r \alpha (1 - \alpha)] = 0 \quad (14)$$

where $\mathbf{U}_r = \mathbf{U}_l - \mathbf{U}_g$. The numerical discretization of the compression term in Eqn. (14) is solved by the velocity flux at the free surface.

$$U_{r,f} = n_f \min \left\{ C_\alpha \frac{|\varphi|}{|S_f|}, \max \left(\frac{|\varphi|}{|S_f|} \right) \right\} \quad (15)$$

where f means the physical quantity in the surface cell, φ the flux, S_f the normal vector of the mesh surface cell, $|S_f|$ the area of mesh surface cells, C_α the compression factor and n_f is the normal vector of free surface.

The surface tension term f_σ in momentum equation is due to the additional pressure gradient generated at the water-gas interface through, which is defined as follow:

$$f_\sigma = \sigma \kappa \nabla \alpha \quad (16)$$

where κ means the average curvature of free surface, and is defined as:

$$\kappa = -\nabla \cdot \left(\frac{\nabla \alpha}{|\nabla \alpha|} \right) \quad (17)$$

The water surface tension coefficient is derived as $\sigma = 0.0734$ in Eqn. (16). More details about VOF method in naoe-FOAM-SJTU solver can be found in Wang et al. (Wang and Wan, 2020)

A finite volume method is used to discretize the computational domain. The pressure-velocity equation is decoupled by the merged PISO-SIMPLE algorithm. The partial differential equations are discretized and solved by several built-in numerical schemes in OpenFOAM. A second-order total variation diminishing limited linear scheme is used to discretize the convection terms and a second-order central

difference scheme is used to approximate the viscous terms.

3. Computational overviews

3.1. Geometry

A surface combatant model DTMB5415 is used for all the numerical computations. The 3D geometry model is shown in Fig. 1, and the main parameters are given in Table 1. The model scale is adopted and the scale ratio is 1:24.824 and the length between the perpendiculars of ship model is 5.72m. This ship model is used as one of the benchmark cases in the Tokyo 2015 CFD Workshop. The experimental data and CFD results about this ship model can be used to compare and verify the result of numerical simulation in this study.

3.2. Computational grids

In this study, commercial software HEXPRESS is used to generate unstructured meshes, and computational domain settings are shown in Fig. 2. Inlet is set at $X = -2L_{pp}$ (L_{pp} is the length between perpendiculars) to simulate ship sailing in clam water with a constant velocity flow, and outlet is set at $X = 3L_{pp}$. A half-domain is used for numerical simulation, and the left, right, and bottom boundaries are set as symmetry. The right boundary is set at $Y = 2L_{pp}$, the bottom boundary is set at $Z = -L_{pp}$, and atmosphere boundary is set at $Z = 0.5L_{pp}$.

Profile view of grid refinement in bow region is shown in Fig. 3, and the mesh refinement in bow wave region is shown in Fig. 4. The specific information of grid refinement is given in Table 2. Mesh refinement is achieved by splitting the cells, where refine level (x, y, z) means that a cell is split into ($2^x, 2^y, 2^z$) cells. Level 0 means that the mesh in this region is not split. Set level (6*6*6) in bow region, level (5*5*5) in transition region. In far field, level (3*3*3) is set to capture wave pattern. In order to better resolve the sharp free surface, mesh is split in Z direction in Fig. 4. Finally, the number of cells of the initial mesh is $90 \times 27 \times 27$ in the x, y, z directions within computational domain while total number of cells after refinement is 10.4 million.

3.3. Test condition

In present work, free surface of breaking bow wave of DTMB5415 is compared under different sailing attitudes. The effects of trim on breaking bow wave features such as plunging jet and air entrainment are analyzed in detail by using CFD method. Since a relatively large bow wave breaking region, stable plunging jet and air entrainment can be clearly observed at $Fr = 0.35$, it is determined that $Fr = 0.35$ represents the best compromise. More details of experimental pictures and test condition under different Fr number can be found in Olivieri et al. (2007).

Firstly, the INSEAN2340 Model test condition (Olivieri et al. (2007)) is selected for the numerical simulation validation. The specific simulation conditions are shown in Table 3 and sinkage and trim are fixed at the experimentally measured values. The accuracy of CFD method is verified by comparing the prediction data such as total resistance, wave pattern and free surface waveform with experimental data.

Then, three sailing attitudes cases, 1 deg for trim by bow, 1 deg for trim by stern and experimental design (all of them rotate along the



Fig. 1. Geometry of DTMB 5415.

Table 1
Main parameters of DTMB5415.

Parameters		Model2340	Full scale
Scale factor	$\lambda(-)$	24.824	1
Length between perpendiculars	$L_{pp}(m)$	5.720	142.0
Beam	$B(m)$	0.760	18.9
Draft	$T(m)$	0.248	6.16
Displacement	$\Delta(tons)$	0.550	8636.0
Displaced volume	$\nabla(m^3)$	0.550	8425.4
Wetted surface area	$S_w(m^2)$	4.786	2949.5

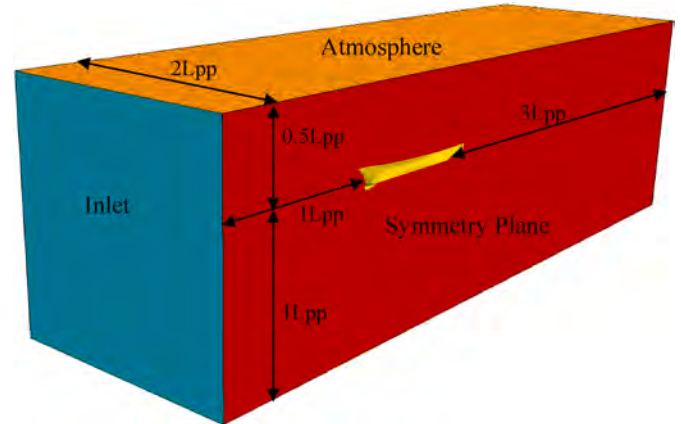


Fig. 2. Computational domain.

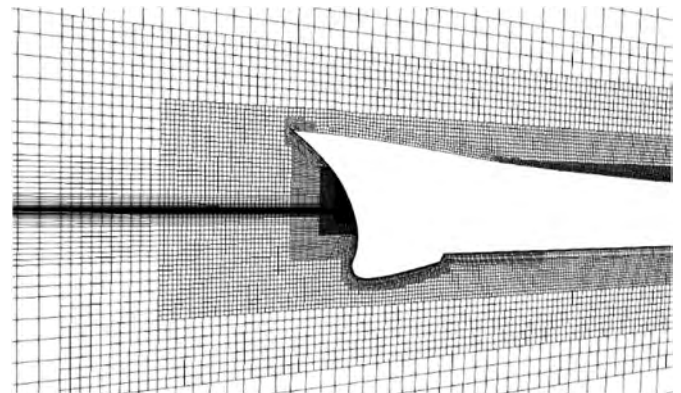


Fig. 3. Profile view of bow region refinement.

counterclockwise and clockwise directions by one deg with the midpoint of the ship bottom as the rotation point) are selected to investigate the breaking bow wave at $Fr = 0.35$. Details about the three cases are given in Table 4 and the geometry in each case is shown in Fig. 5 (The red line is the contour line of the ship bottom in test condition). The physical parameters of water are set as the test condition and given in Table 5. In the latter, trim by bow condition is called as Case1; test design condition as Case2; trim by stern condition is Case3.

In three cases, computations were performed on the HPC cluster at Shanghai Jiao Tong University, with each node consisting of 2 CPUs (Inter Xeon E2680V2, 20 cores per CPU). Three nodes with a total of 120 cores were used to calculate the flow field around the ship hull at $Fr = 0.35$. The time step was set as $\Delta t = 0.001$ s, with the mean Courant number is about 0.7 and maximum Courant number is about 6 for the whole computation domain. The time to complete the computation was approximately 41 wall-clock hours (for one case), with about 25000 time steps for each breaking bow wave simulation. All results are dimensionless with length divided by $L_{pp} = 5.72m$ and velocity divided

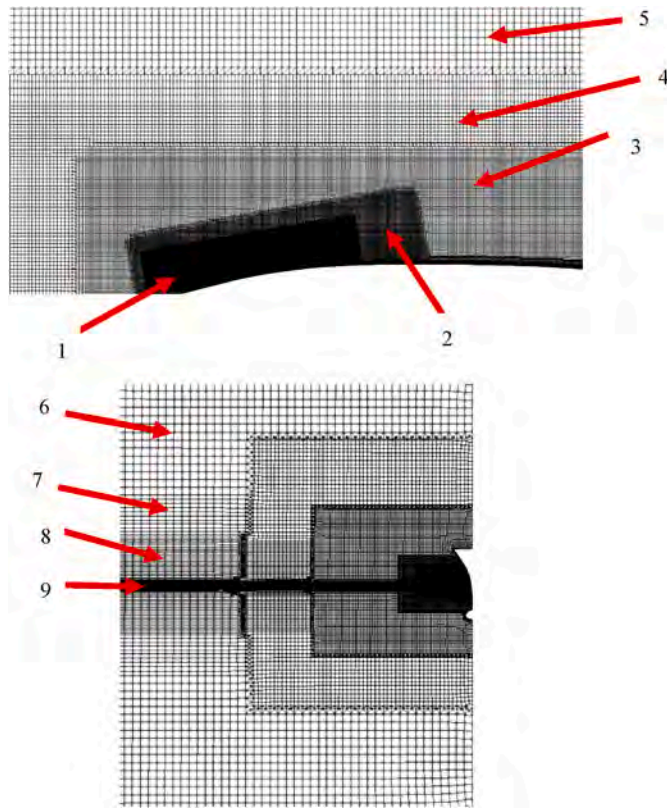


Fig. 4. Mesh refinement in bow wave region.

Table 2
Details of grid refinement.

Block name	Block no.	Refine level (x, y, z)
Bow wave near	1	6*6*6
Bow wave 5th level	2	5*5*5
Bow wave far	3	4*4*4
Far field 3rd level	4	3*3*3
Far field	5	2*2*2
Free surface far	6	0*0*2
Free surface transition	7	0*0*3
Free surface near	8	0*0*4
Free surface 6th level (bow)	9	0*0*6

Table 3
Test conditions.

INSEAN2340	
Speed(m/s)	2.621
Trim(deg)(fixed)	0.069
Sinkage(Lpp)(fixed)	0.0032
Total resistance(N)	80.64
C_m	4.91E-03

Table 4
Draft information for cases.

	Trim angle	Fore draft	Aft draft	Research approach
Case1	1 deg trim by bow	0.2796	0.1798	CFD simulation
Case2	0.069 deg trim by bow	0.2331	0.2262	Numerical verification with test
Case3	1 deg trim by stern	0.1798	0.2796	CFD simulation

by $U = 2.621$ m/s, corresponding to $Fr = 0.35$. The value distribution of $yPlus$ has been checked according to the reviewer's comment, where the $yPlus$ value is around 49.8 at the bow region, and the $yPlus$ value near the stern field is around 35, with a combined average of 37.522. It is concluded that the requirements of the SST $k - \omega$ model of the RANS equation are met.

4. Numerical validation

4.1. Resistance

Predicted resistance in Case2 was validated with the experimental data in this section. Under that set of grids, the viscous force had converged to 24N and pressure resistance remained at about 15N. Resistance coefficients under test condition are shown in Table 6. The total resistance coefficient error is 1.52%. It is concluded that the accuracy of the resistance prediction is considered acceptable in Case2.

4.2. Wave contours

A comparison of the computed wave elevation contours with measurements at $Fr = 0.35$ is shown in Fig. 6. It shows overall good agreement of the wave field and the locations of the scars, which are visible in the bow wave contours. The upper figure is the predicted wave contours obtained in the present work by using DDES method and the bottom figure is the experimental data from Olivieri et al. (2007) It can be observed that the wave height of CFD prediction in the present work is basically the same as the laboratory test, but the scars captured via CFD method are sharper and more obvious than those captured via experimental measurement. A clear wave height gap can be observed and two scars can be visualized by DDES method while the scars measured by EFD method are smoother and no clear gap is visible. However, DES method can capture another scar with the third overpredicted at the end of bow wave front near $Y/Lpp = 0.15$. Fig. 7 shows the comparison of the free surface between the CFD prediction and experimental photographs at $Fr = 0.35$, and the whole bow wave region agrees well with the experimental data.

4.3. Free surface wave field

The predicted mean wave elevation produced by naoe-FOAM-SJTU solver is shown in Fig. 8. It is considered that the breaking bow wave region covers within -0.15 to 0.15 in y direction and the wave height is around 0.2 . The first scar is located at $Y/Lpp = 0.06$ and the second scar is at $Y/Lpp = 0.095$. The first trough is formed at $X/Lpp = 0.24$. The predicted bow, trough, and shoulder wave structures are in good agreement with the experimental measurements.

In Fig. 9, the predicted free surface is compared with the experimental photograph in a close-up view. It can be observed that predicted free surface is relatively smooth. The small-scale free surface features shown in experimental photograph such as free surface turbulence, bubble and spray can hardly be visualized in CFD prediction. A closer analysis of Fig. 9 shows that there is a thin layer of water on the surface of the hull bow, and this layer of water does not separate from the free surface to forms an overflowing breaking bow wave but forms a plunging jet. The plunging jet will fall and touch the free surface below, leading to a stable air entrainment. After that, there is a second overturning plunging jet which is formed followed by a second reconnection. Two localized scars are formed between the air entrainments. These scars extend up to the first wave trough downstream of the bow wave region.

In summary, this section verifies the viability and accuracy of the CFD method via simulation of Case2. The predicted resistance, bow wave contour and free surface formation via CFD method agree well with experiment results. The accurate prediction for the validation case lays a good foundation for the next simulation under different sailing



Fig. 5. DTMB5415 geometry under different sailing attitudes.

Table 5

Water quality.

Water density (kg/m ³)	Kinematic Viscosity (m ² /s)	Surface tension (N/m)	Salinity (<0.5)	Gravity acceleration (m/s ²)	Test temperature (degree centigrade)
998.5	1.09e-6	0.0734	<0.5	9.8033	16.6

Table 6

Comparison of resistance at Fr = 0.35

Resistance	
Speed(m/s)	2.621
C _p	0.001793
C _v	0.003042
C _m	0.004835
C _m (exp)	0.00491
Error	-1.52%

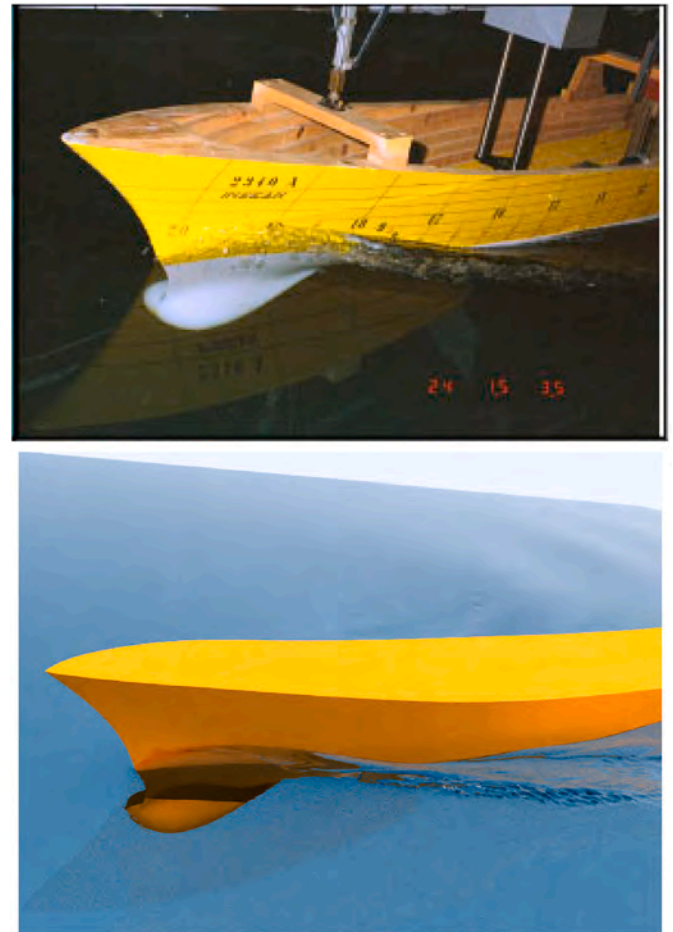


Fig. 7. Comparison of free surface at Fr = 0.35(top: Experiment; bottom: CFD).

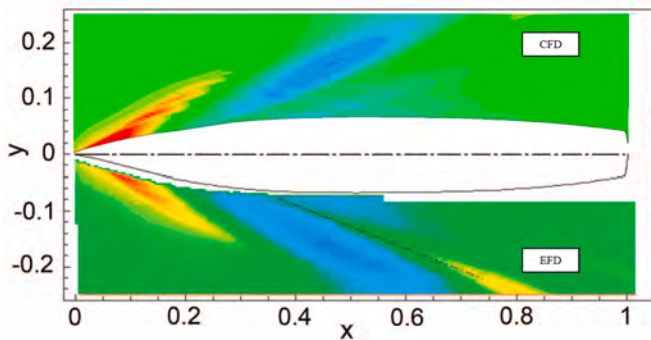


Fig. 6. Comparison of wave contours at Fr = 0.35 (top: DDES bottom: EFD).

attitudes.

5. Trim angle effects

5.1. Resistance

The comparison of resistance in three cases at Fr = 0.35 is shown at Table 7. It can be observed that trim by bow increases the total resistance by 4.49% while trim by stern reduces by 0.893%.

5.2. Wave contour

The wave height curves on hull surface in the three cases are shown

in Fig. 10. The comparison shows that the maximum wave height on the hull surface in Case1 is the highest, while the wave height in Case3 is the lowest, and the wave trough in Case1 is lower than that in Case2 and Case3. From the shape of the curve in Case2, the wave height curve on hull surface is the steepest, indicating that the free surface deformation at trim by bow condition is the most violent among the three cases. And the downstream is also the highest in Case1. In Case3, hull surface wave height curve becomes relatively flat, and the amplitude of both the wave crest and trough are the smallest of those in the three cases. Based on the result from Fig. 10, the wave contour of each case is further compared in Fig. 11. The maximum value of the wave height is artificially set to 0.02, and the color of the wave height exceeding 0.02 is displayed as white.

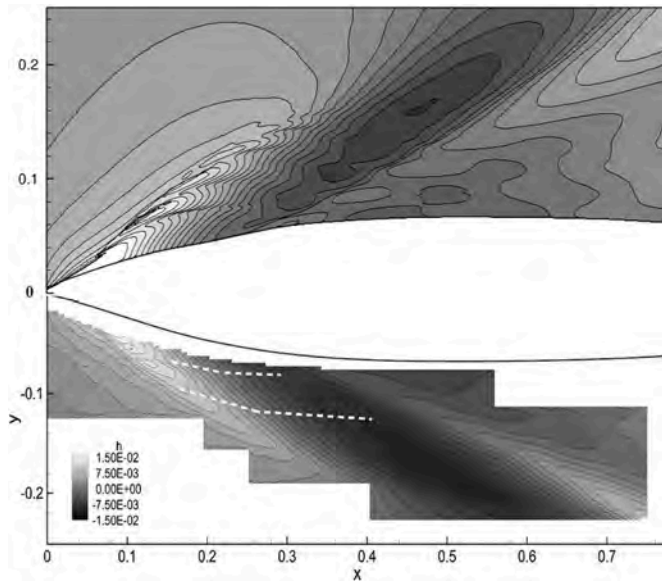


Fig. 8. Comparison of mean wave elevation at $Fr = 0.35$ (top: CFD; bottom: EFD).

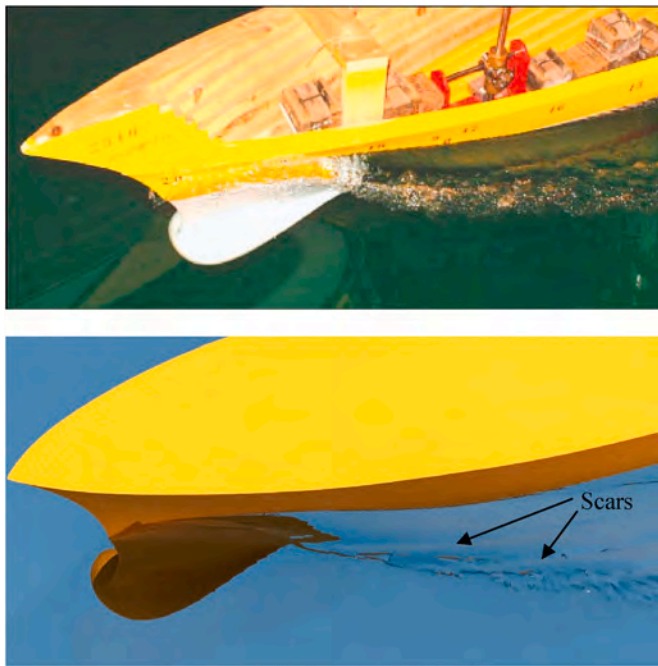


Fig. 9. Comparison of free surface in bow region at $Fr = 0.35$ (close-up).

Table 7
Comparison of resistance in three cases at $Fr = 0.35$

	Pressure Coefficient ($\times 10^{-4}$)	Viscous Coefficient ($\times 10^{-4}$)	Total Coefficient ($\times 10^{-4}$)	Relative Error to Case2 (Total)
Case1	19.40	31.12	50.53	4.49%
Case2	17.93	30.42	48.35	0
Case3	17.02	30.90	47.92	-0.893%

From Fig. 11, in Case1, most of the wave area on the bow region is shown as white, and the second layer of overturned wave is higher and the free surface in the bow region is sharper than that in other cases. In

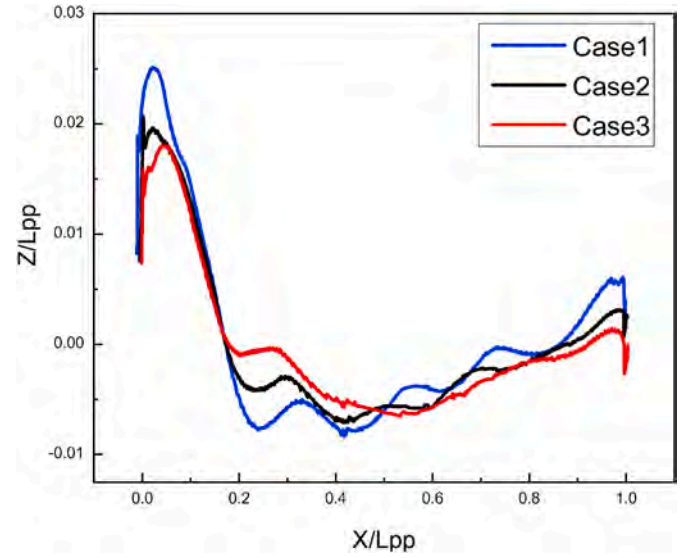


Fig. 10. Comparison of wave height curves on hull surface.

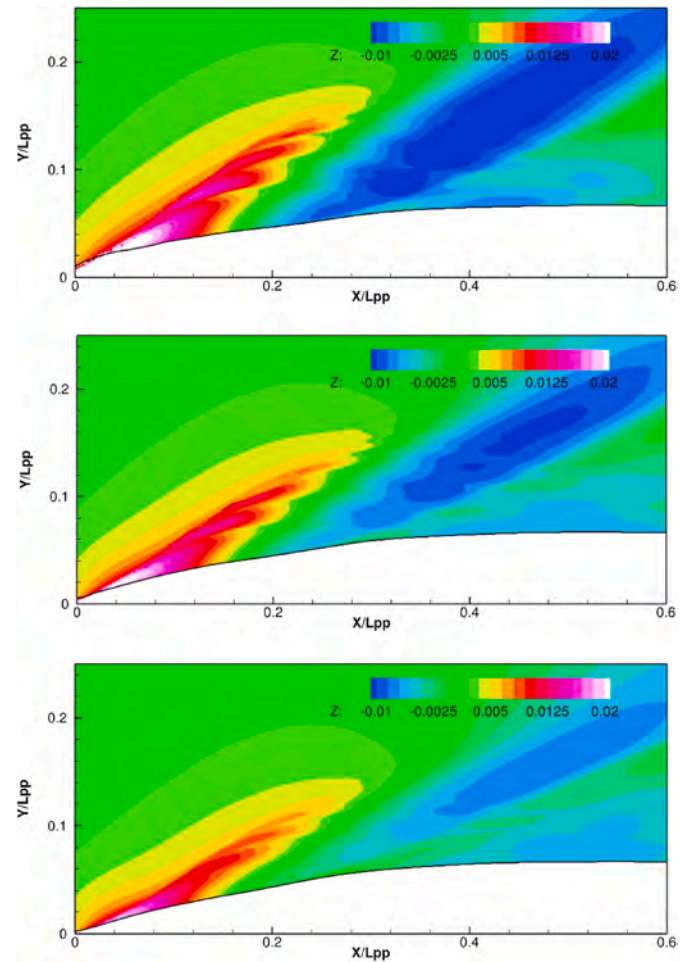


Fig. 11. Comparison of wave contours in the three cases(top: Case1; middle: Case2; bottom: Case3).

Case2, a small portion of white area can be observed in the bow wave region, and the first wave trough is lighter in color. It means that the free surface evolution is not so sharp, but still a significant part of scars can be observed. In Case3, there is no white part on the bow region. The

peaks of the wave crest and trough become smaller, and no obvious scars can be observed. There is no sharp overturned wave on the free surface. In summary, trim by bow sharpens the wave pattern and enlarges the amplitude. By contrast, trim by stern makes the bow wave smoother and the amplitude smaller.

5.3. Free surface wave field

After comparing wave contours at $Fr = 0.35$, the details of free surface evolution and bow wave breaking process are further analyzed. The bow wave region in the close-up perspective is shown in Fig. 12, and the same viewpoint is used to observe the free surface evolution in the three cases. Intuitively, the bow wave height and the second overturned wave height in Case1 are the highest among the three cases. The scars and pocket of air can also be observed in all cases. However, because of the small bow wave height, the energy is not enough to form an overturned wave and a stable pocket of air in Case3.

Fig. 13 shows the comparison of free surface evolution of bow wave breaking in the three cases. The bow wave pattern is shown at various transverse planes from $X/Lpp = 0.05$ to 0.21 . At section $X/Lpp = 0.05$ – 0.11 , the bow wave has completed its first overturning and formed a second plunging jet in the three cases. In Case1 visible plunging jet and stable pocket of air can be observed. In Case2, the first pocket of air disappears and only the plunging jet which is connected to the free surface remains. In Case3, a stable pocket of air is not formed during the first wave overturning. The direction of plunging jet is away from the hull and the velocity in vertical direction is not enough to form the

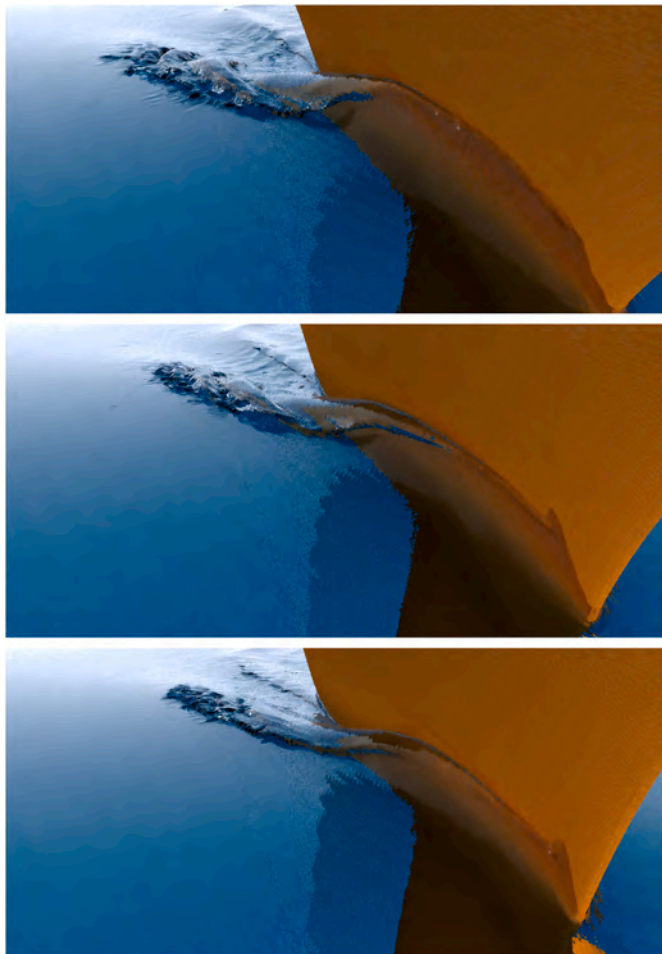


Fig. 12. Close-up view of the bow waves in the three cases (top:Case1; middle: Case2; bottom:Case3).

second overturning at section $X/Lpp = 0.11$, which explains why there is no significant scars in Case3 from Fig. 11. At section $X/Lpp = 0.12$ to 0.21 , the second wave overturning can be observed in Case1 and Case2, and the second plunging jet falls and touches the free surface below, forming a reconnection. When the third plunging jet appears, a second scar is formed. In Case1, even the third overturned wave can be observed, and more than three distinct scars can be visible. While in Case2, the free surface tends to be flat, and there is no bow wave breaking feature after $X/Lpp = 0.15$ cross section.

Intuitively, trim by bow not only makes the free surface of breaking bow wave envelope more sharp, but also makes the wave breaking region bigger and further away from the hull, while the trim by stern makes the region smaller and closer to the hull. In order to get the specific location of the bow wave scars more accurately, the $X/Lpp = 0.1$ section is selected to make a free surface outline as shown in Fig. 14. There is obvious overturned wave and air entrainment in Case1, which is not visible in Case3. Therefore, in this paper, the location of plunging jet generation is selected as the scars for comparative analysis. Comparing the coordinates of the scars and the height of plunging jet in the three cases (Table 8), the Z coordinates of the first scar remain the same in general. In Case1, the Y coordinate of the first scar is about 0.061 away from the hull, and the height of first plunging jet is 0.015. In Case3, the Y coordinate of the first scar is about 0.045 away from the hull, and the height of first plunging jet is 0.011. In summary, compared with the result in Case2, the trim by bow makes the plunging jet higher with the first scar located at 0.010 further from the hull, while the trim by stern makes the plunging jet lower with the first scar located at 0.0055 closer to the hull. It is concluded that trim by bow makes the wave overturning more violent. Conversely, trim by stern smoothen the free surface during bow wave breaking. Different sailing attitudes can affect the height of the bow wave and the position of the scar.

5.4. Flow field analysis

The above conclusion notes that sailing at different attitudes can result in varying free surface outlines and scars positions. It is because of the variation of the wave steep and wave length, which is absolutely affected by the flow field. Therefore, it is considered that the trim changes the initial value of the velocity at the boundary layer near the hull, thereby altering the shape and characteristics of bow wave breaking. In this section, underwater velocity field and vorticity field will be analyzed during bow wave breaking to supplement the experimental data. The effect of different sailing attitudes will be explained through an analysis of the velocity and vorticity distribution around breaking wave region.

5.4.1. Velocity field

Since this paper mainly focuses on the breaking bow wave, there is no planned refinement grid for the shoulder wave region and wake region. The $X/Lpp = 0.15$ cross section is selected to analyze the effect of different trims on underwater velocity field and vorticity field, while the effect of breaking bow waves on the shoulder wave and wake is not considered in this paper. As shown in Fig. 15, the $X/Lpp = 0.15$ section is located in the bow wave breaking region, where the overturning of the two waves have just ended and two distinct scars and a third plunging jet just appear. Comparing the CFD prediction with experimental photograph at $X/Lpp = 0.15$, the CFD prediction has a speed accumulation at the first pocket of air, and a large velocity mutation is observed at the same z coordinate at the bottom of the pocket of air. In the far field, the CFD prediction and experimental photograph both show a tendency to increase in velocity. The level of agreement with the data for the axial velocity contour magnitude and shape is excellent.

The comparison of the transverse velocity fields in the three cases is shown in Fig. 16. It can be observed that the velocity field evolution area is larger in Case1, which means that at the same position such as $z = 0$ and $y = 0.1$, velocity in Case1 is smaller than that in Case2. In Case3,

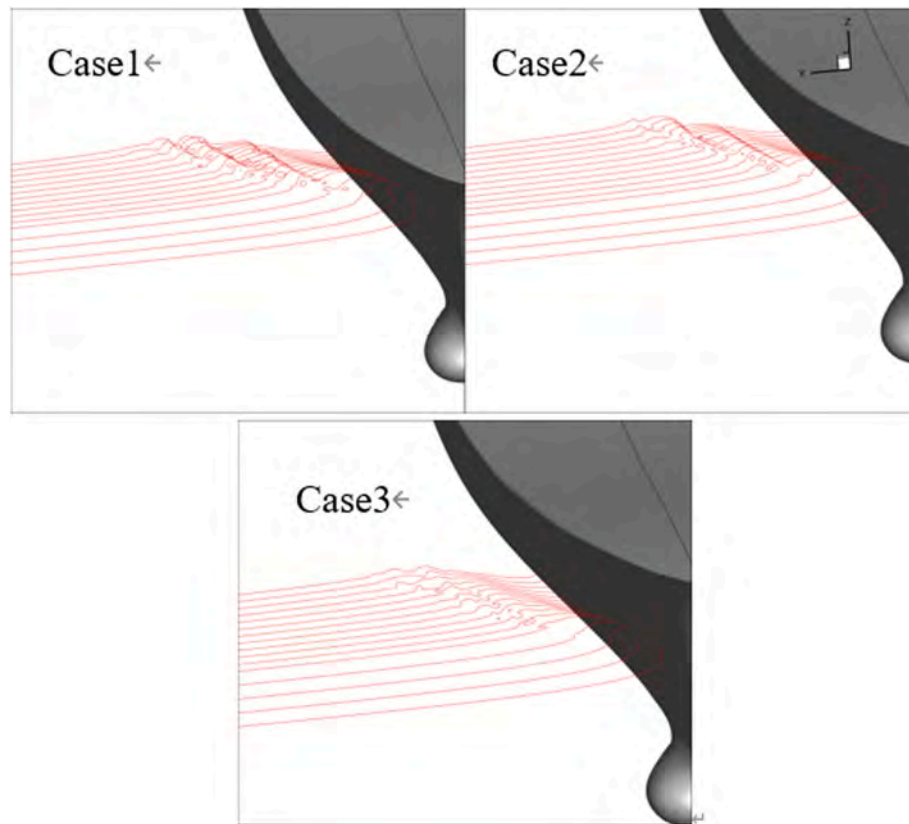


Fig. 13. Comparison of free surface contours from $X/L_{pp} = 0.05$ to 0.21 .

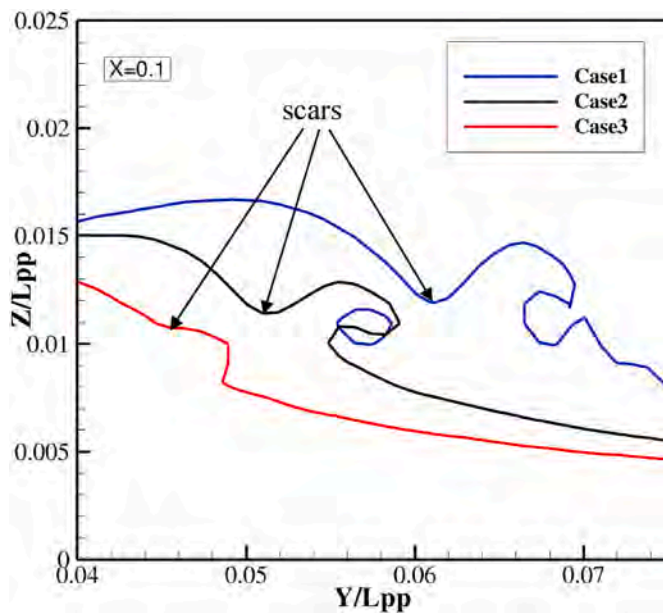


Fig. 14. Comparison of free surface outlines at $X/L_{pp} = 0.1$.

Table 8
Location of the first scar in the three cases.

	Y of the first scar	Z of the first scar	Height of the first plunging jet	Error of Y
Case1	0.06102	0.01193	0.01471	0.01033
Case2	0.05099	0.01142	0.01288	0
Case3	0.04546	0.01075	0.01075	-0.00553

the velocity at the same position is the biggest among the three cases, which nearly becomes incoming flow speed. It can be concluded from the above comparison that trim by bow makes the breaking bow wave region larger, free surface sharper and velocity field evolution area larger. It means that boundary has significant influence on the velocity field in Case1 and the velocity is expected to increase to the inlet speed in a slower manner. However, trim by stern makes the region smaller and free surface flatter, illustrating that boundary has less influence on flow field and thus the velocity increases to the incoming speed faster.

Fig. 17 shows the comparison of longitudinal velocities in the three cases. In Case1, there are more scars observed in the bow wave region, and the more scars mean more vortex and velocity changes. In Case2, since no second overturned wave is generated, the whole velocity field is smoother. The only velocity accumulation is formed near the plunging jet, and the velocity show a tendency to increase outward in rest of the area. In Fig. 18, for the vertical velocity field in Case2, there are two velocity mutations at the first pocket of air near $z = 0$ plane, which is missing in experimental photograph. At the position of plunging jet connected with the second scar, it can be observed that the velocity becomes larger and nearly reaches the maximum speed in z direction. It reflects the basic principle of upward overturning jet during bow wave breaking. In the velocity field in Case1, the overturning waves become more violent, and there is one more scar observed at $y = 0.1$. Near the last scars, a sudden change in velocity occurs. The negative velocity around the second scar transforms into the positive velocity at the third plunging jet. Then the plunging jet falls and touches the free surface below, forming a negative velocity. Finally, there is a third scar appearing and the negative velocity transforms into the positive velocity. This process reflects the variation of the velocity in z direction during the wave overturning, which can also generate vortices at scars.

In summary, this section presents a comparative analysis of the underwater velocity at the $X/L_{pp} = 0.15$ section in the three cases at $Fr = 0.35$. It is concluded that trim by bow enlarges the breaking bow wave

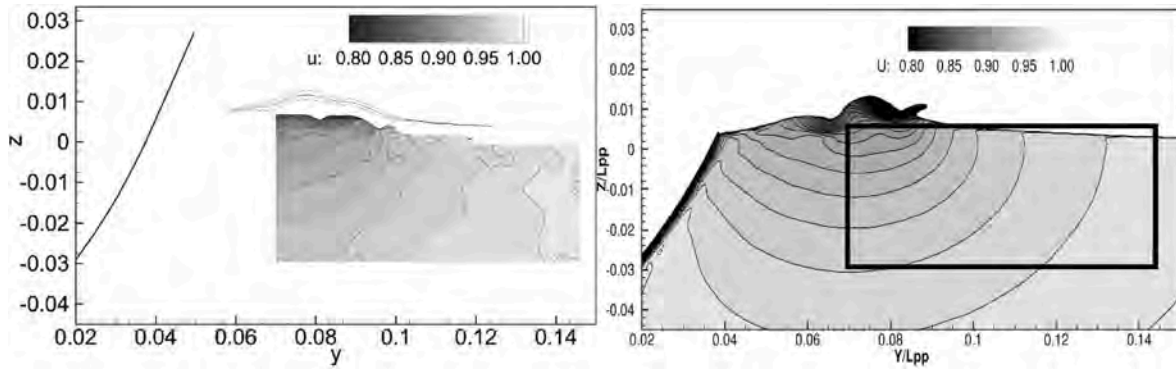


Fig. 15. Comparison of transverse velocity field in Case2 at $X/L_{pp} = 0.15$ (left: EFD; right: Case2).

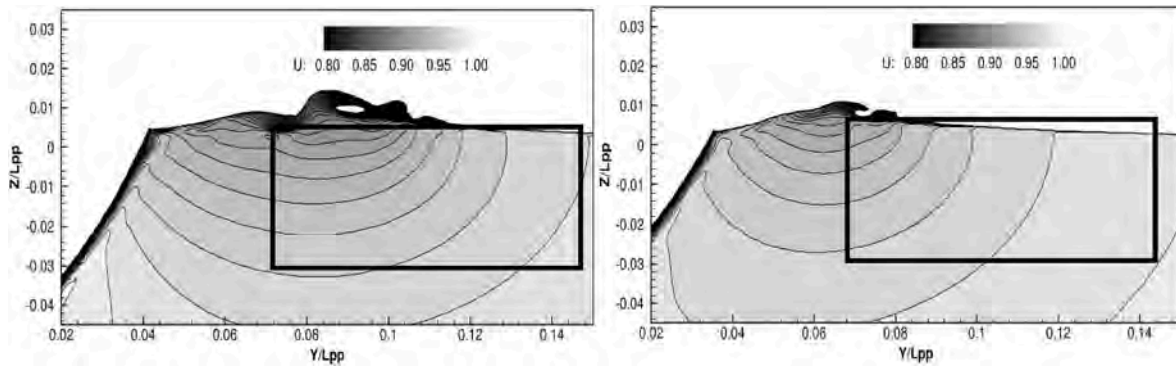


Fig. 16. Comparison of transverse velocity field at $X/L_{pp} = 0.15$ (left: Case1; right: Case3).

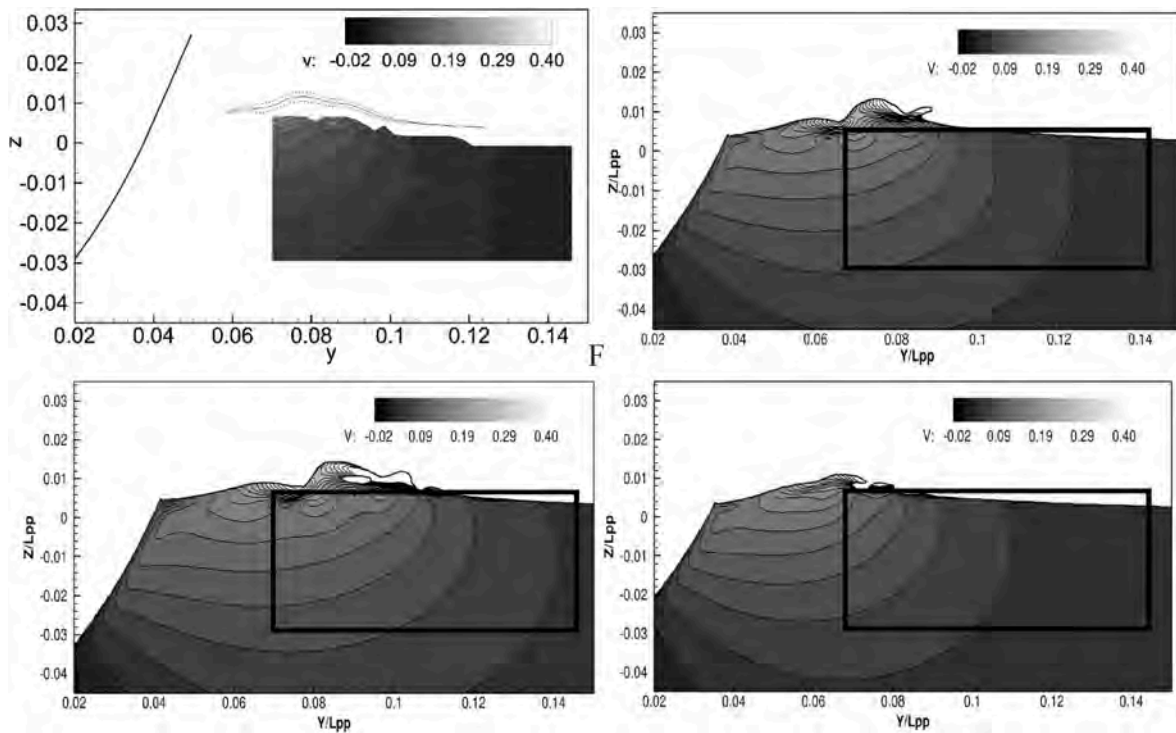


Fig. 17. Comparison of longitudinal velocity field at $X/L_{pp} = 0.15$ (left: Case1; right: Case3).

region while trim by stern decrease the breaking bow wave region. Trim by bow makes the velocity reaching the inlet speed in a slower manner while trim by stern makes it faster. This shows that the boundary

influences more in flow field in the trim by bow case and less in the trim by stern case. Trim by bow generates more scars and more velocity mutations underwater leading to the sharper free surface at the $X/L_{pp} =$

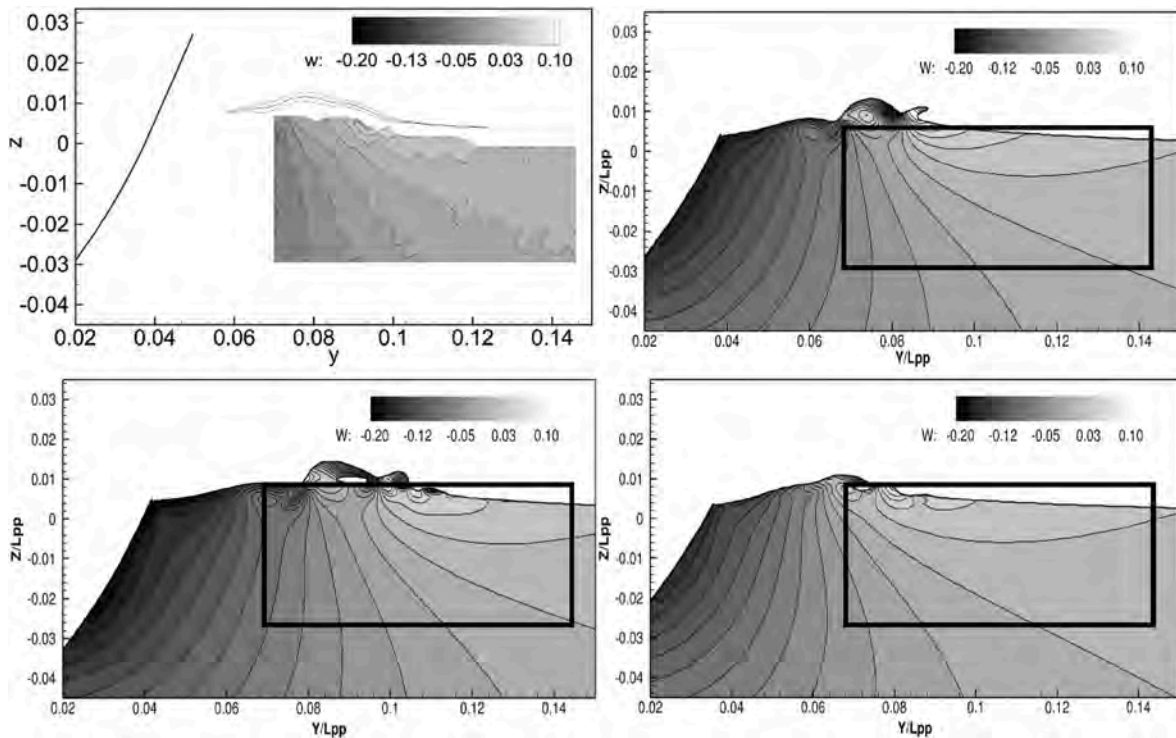


Fig. 18. Comparison of vertical velocity field at $X/L_{pp} = 0.15$ (left: Case1; right: Case3).

0.15 cross section. By contrast, trim by stern smoothen the free surface and the velocity fields in the breaking bow wave region.

5.4.2. Vortical structure

From the conclusion of the previous section, it is clear that bow wave breaking causes drastic free surface evolution, resulting in the variations of the velocity distribution underwater and the generation of vortices. In order to analyze the causes of vortex generation in the breaking bow wave region and the effect of trim on vortex evolution, an iso-surface $Q = 100$ in the bow wave region is taken in Fig. 19. In this section, since the main analysis is the underwater vorticity field during bow wave breaking, the Q from the air part above $\alpha = 0.5$ has been blanked. In

Caes1, trim by bow generates more vortices, which are mainly concentrated on the scars, and a few of vortices appear in the shoulder wave region. It can be observed that the vortices at the position where the bow wave just rises is more obvious. There are more scars vortices in the outward position away from the hull in Case1. However, compared with Case2, the vortices in the downstream area of bow waves are less in Case1. The vorticity in Case3 is smaller in magnitude, and few of vortices can be captured at $Q = 100$ iso-surface. Only a few of vortices exist at scars and no vortices exist in the shoulder wave region. No obvious scars or vortices can be observed in the outward position away from the hull in Case3. It is concluded that trim by bow enlarges the vorticity in scars, which means the wave overturns more violently in

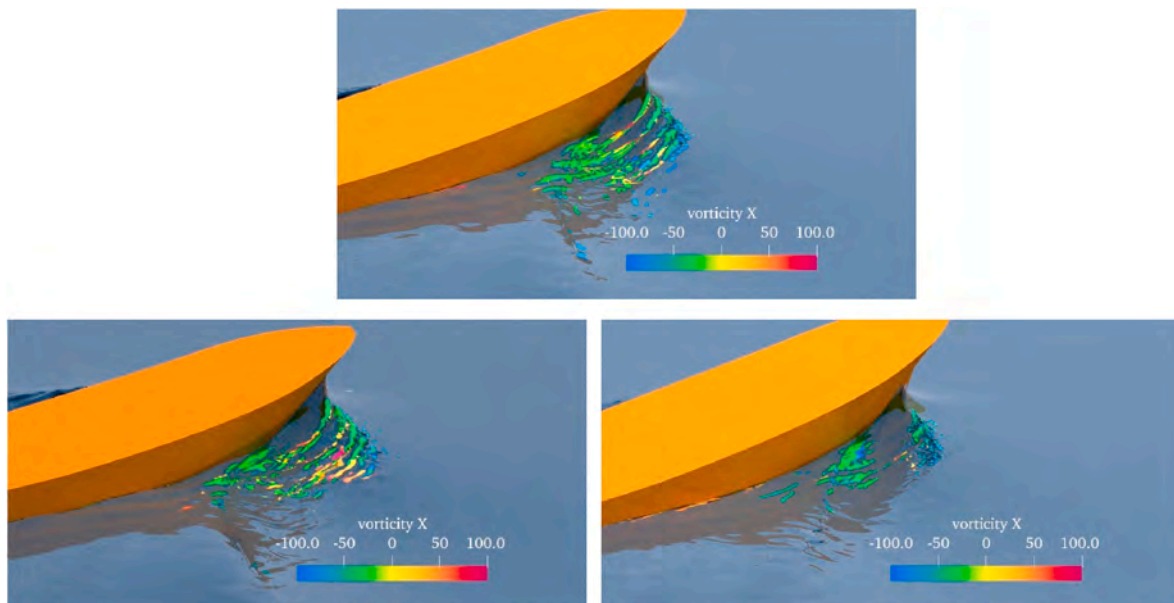


Fig. 19. Comparison of iso-surface $Q = 100$ in the three cases (top:Case2; left:Case1; right:Case3).

trim by bow cases. By contrast, trim by stern reduces the vorticity in the whole bow region.

5.4.3. Initial evolution of bow wave breaking

Intuitively, the intensity, range and the vortex generation of bow wave breaking are directly related to the velocity. For example, the velocity in z direction affects the wave steepness, while the velocity in y direction affects the distance of bow wave scars away from the hull. In order to analyze the effect of velocity on the overturning wave breaking from the principle and the trend of velocity during the overturning process, the turbulent kinetic energy of each cross section is extracted in this part, and the effect of velocity on the breaking bow wave features is characterized by the variation of turbulent kinetic energy. Four cross sections at $X/L_{pp} = 0.05, 0.075, 0.10,$ and 0.15 are selected in this section to compare the vorticity field and turbulent kinetic energy evolution at four cross sections in the three cases.

In Fig. 20, at section $X/L_{pp} = 0.05$, the bow wave appears and the plunging jet has been formed. The wave height in Case1 is larger while that in Case3 is smaller, and there are positive vortices appearing at the hull surface. At $X/L_{pp} = 0.075$, the plunging jet has touched the free surface below, forming a reconnection and ejecting the second plunging jet to form the first scar. There is a stable pocket of air existing at this point. It can be observed that there is a negative vortex V1 near the first air entrainment and a positive vortex V2 above the scars, which interact with each other to form a stable scar. Comparing the vorticity in the three cases, it can be observed that the positive vortices are more obvious in Case1, and the negative vortices mainly accumulates below the first pocket of air and below the second plunging jet. In Case2, the negative vortices show a connection trend, and all of them are below the pocket of air and close to the scar. In Case3, the first pocket of air can hardly be observed, and a few of vortices exist below the scar. At section

$X/L_{pp} = 0.1$, the negative V1 remains at the location of the first pocket of air and moves away from the hull with the evolution of the wave breaking. In Case1, the trim by bow makes V1 move faster and further away from the hull than that in Case2, and the V2 becomes more apparent and is located at the first scar near the second plunging jet. At this time, the second plunging jet has connected with the free surface, forming a second reconnection and generating a negative vortex V3 (below the second air entrainment) and a positive vortex V4 (above the second scars). In Case2, the second overturn has not been completed and V3, V4 cannot be observed. In Case3, it already tends to become spilled breaking wave due to the lack of speed. At $X/L_{pp} = 0.15$, the bow wave breaking has been completed. There are three stable scars and pocket of air formed in Case1, and four negative vortices V1, V3, V5, V7 and three positive vortices V2, V4, V6 can be observed. At this point, V1 and V3 show a tendency to disappear with the evolution of wave overturning. In Case2, the overturning of two bow waves has been completed, and the second pocket of air still remains. Two distinct negative vortices V1, V3 can be observed and the positive vortex V2 becomes smaller with respect to the $X/L_{pp} = 0.1$ cross section. In Case3, the negative vortex V1 cannot be captured and the energy is not enough to form an overturned wave. The wave illustrates that the formation of spilled wave breaking continues to evolve.

In Fig. 21, at section $X/L_{pp} = 0.05$, there is small values of turbulent kinetic energy above the plunging jet at the initial formation of the bow wave, indicating that the velocity of the plunging jet is high and the jet tends to slam downward. Turbulent kinetic energy is also presented at the free surface below the plunging jet, which indicates that liquid flows back below the jet in order to maintain mass conservation. In comparison, the turbulent kinetic energy range of the free surface below the head is larger in Case1, while no significant turbulent kinetic energy variation is observed below the plunging jet in Case3. At section X/L_{pp}

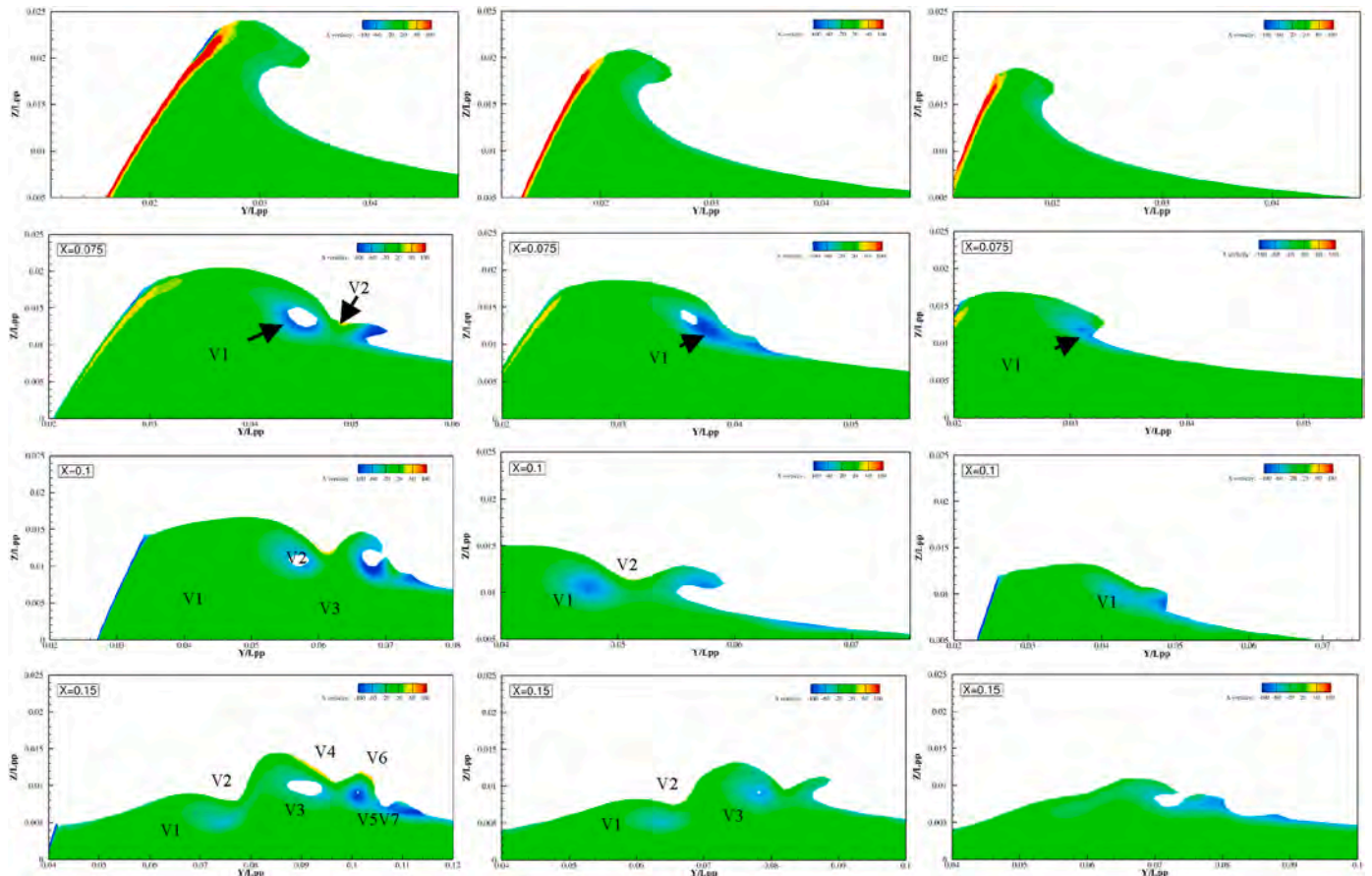


Fig. 20. Axial vorticity distribution during bow wave breaking(left:Case1; middle:Case2; right:Case3).

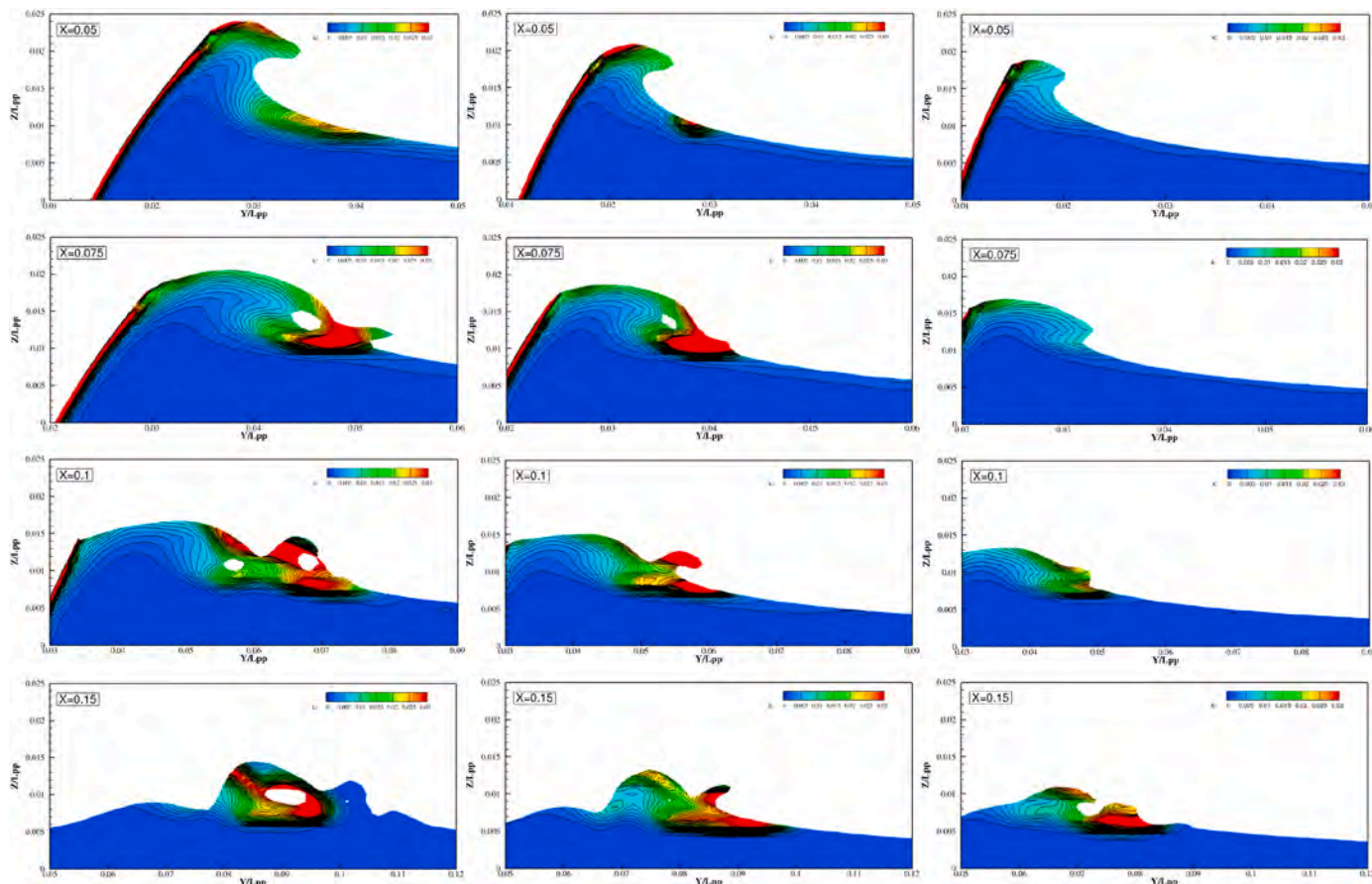


Fig. 21. Evolution of turbulent kinetic energy(left:Case1; middle:Case2; right:Case3).

$= 0.075$, the plunging jet hits the free surface and forms a pocket of air. At this time, the turbulent kinetic energy at the scars becomes significantly larger, suggesting that an ejected water jet will be produced subsequently, forming a second overturned wave. At section $X/Lpp = 0.1$, the second plunging jet appears, carrying a large amount of turbulent kinetic energy. The second wave overturning has been completed in Case1, the whole wave shows a trend away from the hull, and the turbulent kinetic energy is larger in general in the bow wave region. In contrast, there is less energetic and turbulent kinetic energy in Case3, so it cannot form an ejected water jet at this point. At section $X/Lpp = 0.15$, in Case1, there is a second pocket of air formed, with a large velocity accumulation. In Case2, the turbulent kinetic energy at the jet is larger, and the jet can continue to form another overturned wave, while the turbulent kinetic energy in Case3 only supports the movement of the wave away from the hull and does not support the formation of bow wave breaking, which is consistent with the conclusion of the vortex analysis in the above paragraph.

In summary, trim by bow increases the wave turbulent kinetic energy, enlarges the wave height, lengthens the wave length and makes the underwater vorticity larger at the same position. In trim by bow condition, the wave has more energy to complete the overturning and advance, and more stable vortices are formed at the pocket of air. Conversely, trim by stern reduces the wave turbulent kinetic energy, so that the wave does not have enough energy to complete the bow wave breaking and the free surface thus remains flat and the vorticity becomes smaller in trim by stern condition.

6. Conclusions

In this paper, the bow wave breaking phenomenon of benchmark model DTMB5415 at $Fr = 0.35$ is simulated based on naoe-FOAM-SJTU

solver, with focus on the effect of trim on breaking bow waves. The resistance, wave contour, vorticity field, velocity field and turbulent kinetic energy have been studied under 1 deg trim by bow condition and 1 deg trim by stern condition via DDES method. Details in flow field and analysis of the initial evolution of breaking bow wave have been provided. The main conclusions of this paper are given as follows.

A CFD simulation of breaking bow wave was carried out and the predicted results were validated with the experimental data. The predicted total resistance coefficient is only underestimated by 1.52%. It is proved that the accuracy of the resistance prediction is considered acceptable. In terms of wave contours, the predicted wave contours in this paper are consistent with the experimental photographs and the predicted bow, trough, and shoulder wave structures are in good agreement with the experimental measurements.

Comparing the total resistance under the three cases, it can be observed that trim by bow increases the total resistance by 4.49% while trim by stern reduces by 0.893%. In respect of wave height, the $Z = 0.02Lpp$ is used as the reference to compare the bow wave height in the three cases, and the wave height on the surface of the hull is extracted for comparison. In summary, trim by bow sharpens the wave pattern and enlarges the amplitude. By contrast, trim by stern makes the bow wave smoother and the amplitude smaller. It is obvious that trim by bow enlarges the wave breaking region and makes scars further away from the hull. While the opposite conclusion was reached in trim by stern condition by comparing the free surface in a close-up view. The free surface waveforms at the $X/Lpp = 0.1$ section in the three cases is extracted for comparison. The results show that the position of the Z coordinate of the first scar remains the same in all three cases and trim by bow enlarges the plunging jet height with the first scar positioned further from the hull. By contrast, the opposite result is obtained for trim by stern condition.

The distribution of underwater velocity field at $X/L_{pp} = 0.15$ section shows that trim by bow enlarges the breaking bow wave region while trim by stern makes the breaking bow wave region smaller. Trim by bow makes the velocity increasing to the inlet speed in a slower manner while trim by stern makes it faster conversely, which means that the boundary has more influence on the flow field in the trim by bow case than in the trim by stern case. In terms of vortex structure, it is concluded that trim by bow enlarges the vorticity in scars, which means the wave overturns more violently in the trim by bow cases. On the contrary, trim by stern reduces the vorticity in the whole bow region. The processes of the initial evolution of bow wave breaking are analyzed. It is found that trim by bow increases the wave turbulent kinetic energy, enlarges the wave height, lengthens the wave length and makes the underwater vorticity larger at the same position. In trim by bow condition, the wave has more energy to complete the overturning and advance, and more stable vortices are formed at the pocket of air. By contrast, trim by stern decreases the wave turbulent kinetic energy, so that the wave does not have enough energy to complete the bow wave breaking and the free surface evolves flat and the vorticity becomes smaller in trim by stern condition.

The present work verified the reliability of the numerical method and studied the influence of trim on breaking bow wave by analyzing the details of flow field in the bow region, which can also provide guidance for benchmark measurements and fill in the gap of the experimental data. In future work, more cases under different Fr number will be simulated to analyze the effect of speed on breaking bow wave, and the reason of the overpredicted scars captured by DDES method will be further studied.

Data availability

The data that support the findings of this study are available from the corresponding author upon reasonable request.

CRedit authorship contribution statement

Dingkun Wu: Data curation, Writing – original draft, preparation, Visualization, Investigation, Software, Validation. **Jianhua Wang:** Software, Data curation, Visualization, Investigation, Validation. **Decheng Wan:** Supervision, Conceptualization, Methodology, Investigation, Writing – review & editing.

Declaration of competing interest

The authors declare the following financial interests/personal relationships which may be considered as potential competing interests: Decheng Wan reports financial support was provided by Shanghai Jiao Tong University.

Acknowledgments

This work is supported by National Natural Science Foundation of

China (52131102, 51879159), and the National Key Research and Development Program of China (2019YFB1704200), and to which the authors are most grateful.

References

- Bhushan, S., Alam, M., Walters, D., 2013. Evaluation of hybrid RANS/LES models for prediction of flow around surface combatant and Suboff geometries[J]. *Comput. Fluid 88*, 834–849.
- Carrica, P., Huang, J., Noack, R., Kaushik, D., Smith, B., Stern, F., 2010. Large-scale DES computations of the forward speed diffraction and pitch and heave problems for a surface combatant[J]. *Comput. Fluid 39* (7), 1095–1111.
- Deike, L., Popinet, S., Melville, W.K., Cambridge University Press (CUP), 2015. Capillary effects on wave breaking[J]. *J. Fluid Mech. 769*, 541–569, 2015.
- Dong, R.R., Katz, J., Huang, T.T., Cambridge University Press, 1997. On the structure of bow waves on a ship model[J]. *J. Fluid Mech. 346*, 77–115, 1997.
- Kornev, N., Shevchuk, I., Abbas, N., Anschau, P., Samarbaksh, S., 2019. Potential and limitations of scale resolved simulations for ship hydrodynamics applications[J]. *Ship Technol. Res. 66* (2), 83–96.
- Le, T.H., Vu, M.T., Bich, V.N., Phuong, N.K., Ha, N.T.H., Chuan, T.Q., Tu, T.N., 2021. Numerical investigation on the effect of trim on ship resistance by RANSE method [J]. *Appl. Ocean Res. 111*, 102642.
- Li, J., Yuan, B., Carrica, P.M., 2020. Modeling bubble entrainment and transport for ship wakes: progress using hybrid RANS/LES methods[J]. *J. Ship Res. 64* (4), 328–345.
- Liu, Z., Liu, W., Chen, Q., Luo, F., Zhai, S., 2020. Resistance reduction technology research of high speed ships based on a new type of bow appendage[J]. *Ocean Eng. 206*, 107246.
- Menter, F.R., Kuntz, M., Langtry, R., 2003. Ten years of industrial experience with the SST turbulence model[J]. *Heat Mass Tran. 4*.
- Olivieri, A., Pistani, F., Mascio, A.D., 2003. Breaking wave at the bow of a fast displacement ship model[J]. *J. Mar. Sci. Technol. 8* (2), 68–75.
- Olivieri, A., Pistani, F., Wilson, R., Campana, E.F., Stern, F., 2007. Scars and vortices induced by ship bow and shoulder wave breaking[J]. *J. Fluid Eng. 129* (11), 1445–1459.
- Ren Z, Wang J, Wan DC. Numerical simulation of ship bow wave breaking using DES and RANS[C]. *The 9th International Conference on Computational Methods (ICCM2018)*, 06-10 August 2018, Rome, Italy, pp.1001-1012.
- Sherbaz, S., Duan, W., 2014. Ship trim optimization: assessment of influence of trim on resistance of MOERI container ship.[J]. *Sci. World J. 2014* (8), 603695, 603695.
- Wang, J., Wan, D.C., 2017. Breaking wave simulations of high-speed surface combatant using OpenFOAM[C]. In: *Proceedings of the 8th International Conference on Computational Methods. ICCM2017*, pp. 25–29.
- Wang, J., Wan, D.C., 2018. CFD investigations of ship maneuvering in waves using naoe-FOAM-SJTU Solver[J]. *J. Mar. Sci. Appl. 17* (3), 443–458.
- Wang, J., Wan, D.C., 2019. Numerical simulations of viscous flows around JBC ship using different turbulence models[C]. In: *The 11th International Workshop on Ship and Marine Hydrodynamics*, pp. 22–25. Hamburg, Germany, September.
- Wang, J., Wan, D.C., 2020. Application progress of computational fluid dynamic techniques for complex viscous flows in ship and ocean engineering[J]. *J. Mar. Sci. Appl. 19*, 1–16.
- Wang, J., Zhao, W., Wan, D.C., 2019. Development of naoe-FOAM-SJTU solver based on OpenFOAM for marine hydrodynamics[J]. *J. Hydrodyn. 31* (1), 1–20.
- Wang, J., Ren, Z., Wan, D.C., others, 2020. Study of a container ship with breaking waves at high Froude number using URANS and DDES methods[J]. *J. Ship Res. 64* (4), 346–356.
- Wilson, R.V., Carrica, P.M., Stern, F., 2007. Simulation of ship breaking bow waves and induced vortices and scars[J]. *Int. J. Numer. Methods Fluid. 54* (4), 419–451.
- Zhao, W., Wan, D.C., 2016. Detached-eddy simulation of flow past tandem cylinders.[J]. *Appl. Math. Mech. 37* (12), 1272–1281.
- Zhao, W., Wang, J., Wan, D.C., 2020. Vortex identification methods in marine hydrodynamics[J]. *J. Hydrodyn. 32* (2), 286–295.